



OPEN ACCESS

HETDEX Public Source Catalog 1—Stacking 50,000 Lyman Alpha Emitters*

Dustin Davis¹ , Karl Gebhardt¹ , Erin Mentuch Cooper¹ , William P. Bowman² , Barbara Garcia Castanheira³, John Chisholm¹ , Robin Ciardullo^{4,5} , Maximilian Fabricius^{6,7} , Daniel J. Farrow^{8,9} , Steven L. Finkelstein¹ , Caryl Gronwall^{4,5} , Eric Gawiser¹⁰ , Gary J. Hill^{1,11} , Ulrich Hopp^{6,7} , Lindsay R. House¹ , Donghui Jeong^{4,5} , Wolfram Kollatschny¹² , Eiichiro Komatsu^{13,14} , Chenxu Liu^{1,15} , Maja Lujan Niemeyer¹³ , Alberto Saldana-Lopez¹⁶ , Shun Saito^{14,17} , Donald P. Schneider^{4,5} , Jan Snigula^{6,7} , Sarah Tuttle¹⁸ , Laurel H. Weiss¹ , Lutz Wisotzki¹⁹, and Gregory Zeimann²⁰

¹ Department of Astronomy, The University of Texas at Austin, Austin, TX 78712, USA

² Department of Astronomy, Yale University, New Haven, CT 06520, USA

³ Department of Physics, Baylor University, Waco TX 76798, USA

⁴ Department of Astronomy & Astrophysics, The Pennsylvania State University, University Park, PA 16802, USA

⁵ Institute for Gravitation and the Cosmos, The Pennsylvania State University, University Park, PA 16802, USA

⁶ Max-Planck Institut für extraterrestrische Physik, Giessenbachstrasse 1, D-85748 Garching, Germany

⁷ Fakultät für Physik, Universitäts-Sternwarte, Ludwig-Maximilians-Universität München, Scheinerstraße 1, D-81679 München, Germany

⁸ Centre of Excellence for Data Science, Artificial Intelligence and Modelling (DAIM), University of Hull, Cottingham Road, Kingston-upon-Hull, HU6 7RX, UK

⁹ E.A. Milne Centre for Astrophysics, University of Hull, Cottingham Road, Kingston-upon-Hull, HU6 7RX, UK

¹⁰ Department of Physics & Astronomy, Rutgers, The State University of New Jersey, Piscataway, NJ 08854, USA

¹¹ McDonald Observatory, The University of Texas at Austin, Austin, TX 78712, USA

¹² Institut für Astrophysik, Universität Göttingen, Friedrich-Hund-Platz 1, D-37077 Göttingen, Germany

¹³ Max-Planck-Institut für Astrophysik, Karl-Schwarzschild-Straße 1, D-85748 Garching, Germany

¹⁴ Kavli Institute for the Physics and Mathematics of the Universe (WPI), Todai Institutes for Advanced Study, The University of Tokyo, Kashiwanoha, Kashiwa, Chiba 277-8583, Japan

¹⁵ South-Western Institute for Astronomy Research, Yunnan University, Kunming, Yunnan, 650500, Peoples Republic of China

¹⁶ Department of Astronomy, University of Geneva, 51 Chemin Pegasi, 1290 Versoix, Switzerland

¹⁷ Institute for Multi-messenger Astrophysics and Cosmology, Department of Physics, Missouri University of Science and Technology, 1315 N. Pine Street, Rolla, MO 65409, USA

¹⁸ Department of Astronomy, University of Washington, Seattle, 3910 15th Avenue NE, Room C319, Seattle, WA 98195-0002, USA

¹⁹ Leibniz-Institut für Astrophysik Potsdam (AIP), An der Sternwarte 16, D-14482 Potsdam, Germany

²⁰ Hobby Eberly Telescope, The University of Texas at Austin, Austin, TX, 78712, USA

Received 2023 February 22; revised 2023 June 13; accepted 2023 July 2; published 2023 September 7

Abstract

We describe the ensemble properties of the $1.9 < z < 3.5$ Lyman alpha emitters (LAEs) found in the HETDEX survey’s first public data release, HETDEX Public Source Catalog 1. Stacking the low-resolution ($R \sim 800$) spectra greatly increases the signal-to-noise ratio (S/N), revealing spectral features otherwise hidden by noise, and we show that the stacked spectrum is representative of an average member of the set. The flux-limited, $\text{Ly}\alpha$ S/N restricted stack of 50,000 HETDEX LAEs shows the ensemble biweight *average* $z \sim 2.6$ LAE to be a blue (UV continuum slope ~ -2.4 and $E(B - V) < 0.1$), moderately bright ($M_{\text{UV}} \sim -19.7$) star-forming galaxy with strong $\text{Ly}\alpha$ emission ($\log L_{\text{Ly}\alpha} \sim 42.8$ and $W_{\lambda}(\text{Ly}\alpha) \sim 114 \text{ \AA}$), and potentially significant leakage of ionizing radiation. The rest-frame UV light is dominated by a young, metal-poor stellar population with an average age of 5–15 Myr and metallicity of $0.2\text{--}0.3 Z_{\odot}$.

Unified Astronomy Thesaurus concepts: Catalogs (205); Emission line galaxies (459); Lyman-alpha galaxies (978); Redshift surveys (1378)

Supporting material: data behind figures

1. Introduction

The Hobby–Eberly Telescope Dark Energy Experiment (HETDEX; Gebhardt et al. 2021; Hill et al. 2021) is a multiyear, untargeted, low-resolution ($R \sim 800$) spectroscopic survey conducted with the Hobby–Eberly Telescope (HET;

Ramsey et al. 1998; Hill et al. 2021) and the Visible Integral-field Replicable Unit Spectrograph (VIRUS; Hill et al. 2021). Object spectra are identified post-observation via examination of the spatial and spectral clustering of the individual optical spectra from the $\sim 35,000$ fibers in the array (Section 2). The HETDEX Public Source Catalog 1, hereafter HPSC-1 (Mentuch Cooper et al. 2023), contains spectra for more than 200,000 objects from the first 3 yr of HETDEX observations. Within this data set are more than 50,000 Lyman alpha emitting (LAE) galaxies at $1.9 < z < 3.5$ identified by their $\text{Ly}\alpha$ emission lines, which HETDEX is specifically designed to detect. Using the 3D positions of these LAEs, which serve as biased mass tracers, HETDEX aims to constrain the Hubble parameter, $H(z)$, and the angular diameter distance, $D_A(z)$, at $z \sim 2.4$ to better than 1% accuracy (Gebhardt et al. 2021). The success of this primary science goal is predicated on the accurate measurement of the

* Based on observations obtained with the Hobby-Eberly Telescope, which is a joint project of the University of Texas at Austin, the Pennsylvania State University, Ludwig-Maximilians-Universität München, and Georg-August-Universität Göttingen. The HET is named in honor of its principal benefactors, William P. Hobby and Robert E. Eberly.



Original content from this work may be used under the terms of the [Creative Commons Attribution 4.0 licence](#). Any further distribution of this work must maintain attribution to the author(s) and the title of the work, journal citation and DOI.

redshifts, and hence the correct identification of the Ly α emission line, of the roughly 1 million LAEs out of the several million total galaxies and other astrophysical sources expected to be observed over the course of the HETDEX survey. The spectra obtained from the untargeted observations are exploited to this end (Davis et al. 2023).

The HETDEX spectral range is 3500–5500 Å with $\lambda/\Delta\lambda \sim 800$ (Hill et al. 2021). Most, $\sim 80\%$, of all HETDEX emission-line detections (or $\sim 70\%$ of all HETDEX objects when including those identified from their continuum rather than emission lines) are in spectra without significantly detected continua and thus provide very little extra information beyond their emission-line-specified redshifts. However, with the classifications and redshifts of these objects known to high precision and with little misidentification, especially for Ly α (only $\sim 2\%$ of all identified Ly α emission lines are not Ly α (Davis et al. 2023), it becomes practical to stack the spectra to explore the average properties of subpopulations of galaxies (specifically LAEs, for this work). Throughout this paper, we use the biweight measure of the central location²¹ (Beers et al. 1990) as a measure of the average properties in the stack. This is very similar to the median in the limit of a large sample size, such as presented here (see also Section 3.4), but provides an improved robustness to outliers, particularly when the sample distribution is non-Gaussian. When the sample is Gaussian-like, the difference is $\ll 1\%$. For simple comparisons and convenience, the mean or median and standard deviation may also be used, but are explicitly identified.

Here we define LAE to mean $1.88 < z < 3.52$ galaxies that do not host active galactic nuclei (AGNs). With the HETDEX emission-line search, these galaxies are nearly all ($\gtrsim 96\%$) classical LAEs by definition of a 20 Å or greater rest-frame equivalent width Ly α emission (Gronwall et al. 2007; Adams et al. 2011). Only a relative few of these LAEs have sufficiently bright continua to be selected as Lyman break galaxies (LBGs; Guhathakurta et al. 1990; Madau et al. 1996; Steidel et al. 1996; Shapley et al. 2003). Generally, the LAEs in the HETDEX redshift window are compact, low-metallicity, rapidly star-forming galaxies (Gawiser et al. 2007; Nilsson & Meisenheimer 2009; Finkelstein 2010, and many others).

The stacking of spectra, whether for LAEs or other phenomena, is not new (Green et al. 1996; Hu et al. 2005; Balestra et al. 2010; Berry et al. 2012; Jaskot & Oey 2014; Grazian et al. 2016; Steidel et al. 2018; Feltre et al. 2020, and many others). HETDEX is unusual in its lack of preselection coupled with the large number of available spectra, which will number in the millions by the end of the survey. High-quality spectral observations of individual $z > 2$ galaxies remain extremely rare and limit our ability to extrapolate to a population description, where stacking, by its statistical nature, describes population features.

The large number of spectra from the observations included in HPSC-1 (which contains roughly a quarter of the planned 540 deg² sky coverage of the full HETDEX survey; Gebhardt et al. 2021; Mentuch Cooper et al. 2023) provide significant statistical leverage. Given the untargeted nature of the HETDEX observations and assuming the spectra are down selected without significant restriction on their on-sky locations, the stacks are largely unbiased with respect to the LAEs' environments. Additionally, these statistically large stacks

marginalize over galaxy orientation, dust geometry, star formation stochasticity, and lines of sight through the intergalactic medium (IGM). That last marginalization allows for a more straightforward application of IGM attenuation corrections, which are inherently statistical averages (Meiksin 2006; Byrohl & Gronke 2020; Bassett et al. 2022), while the other properties embody the random variability in the galaxy population, and in particular, their radiative transfer processes (Heckman et al. 2011; Leitet et al. 2013; Steidel et al. 2018; Saldana-Lopez et al. 2022; Smith et al. 2022). Further, with 10,000–50,000 spectra in each of the stacks in this work, the signal-to-noise ratio (S/N) is boosted by a factor of 100 or more. This makes possible the measure of signal that is otherwise buried in noise for individual spectra.

In this work, we stack subsamples of the HPSC-1 spectra to explore the basic ensemble properties of $1.9 < z < 3.5$ LAEs and preview future analyses using even larger collections of HETDEX spectra.

The remainder of this paper is organized as follows. Section 2 briefly describes the HETDEX observations and reduction pipeline. Section 3 provides an overview of the selection and stacking mechanics. Section 4 presents the results and discusses the various explored properties of the data sets.

Throughout the paper, the Planck 2018 cosmology (Aghanim et al. 2020) with $\Omega_m = 0.31$ and $H_0 = 67.7$ km s⁻¹ Mpc⁻¹ is assumed. All magnitudes are in the AB system.

2. Observations and Data Selection

For a more thorough and complete description of the HETDEX observations, data reduction, and the particular composition of HPSC-1, we refer the readers to Gebhardt et al. (2021) and Mentuch Cooper et al. (2023).

In brief, HETDEX is a multiyear spectroscopic survey conducted at the McDonald Observatory with the 10 m HET. Observations began in 2017 and will continue through 2024 with a planned coverage of some 540 deg² in two large fields pointing out of the Galactic plane, one centered near 193°+53° and the other near 22°+0°. Pointings within the two fields are untargeted, and the spectra are collected with up to 78 pairs of integral field unit (IFU) spectrographs in VIRUS spread out over the HET's focal plane with a fill factor of 1:4.5. Each IFU is fed by 448 fibers (Hill et al. 2021) and each observation consists of three exposures of 6.1 minute duration that are dithered to fill in the coverage within the IFU footprints. The resulting spectra, $\sim 33,000$ per observation, are calibrated, sky subtracted, and scanned for emission lines (or continua) without any color or magnitude preselection, and, where lines (or continua) are found, the spectra from the surrounding fibers inside a 3.5" radius aperture are combined into a single, point-spread function (PSF) weighted spectrum (Gebhardt et al. 2021). Though the apertures are large, for the 1.7" average seeing FWHM, 90% of the light for the spectrum comes from the innermost 1.2".

The PSF-weighted spectra are classified and assigned a redshift with the ELiXer software (Davis et al. 2023)²² using multiple analyses and incorporating archival photometric imaging. Brighter ($g < 22$) spectra are classified with support from Diagnose²³, a software package developed for the

²¹ Also known as the *biweight location*; also referred to as the *biweight average* or just the *biweight* in this and other works.

²² The HPSC-1 classifications derive from an earlier version of the ELiXer software than is presented in Davis et al. (2023).

²³ <https://github.com/grzeimann/Diagnose>

Hobby-Eberly Telescope VIRUS Parallel Survey, which is based on template fitting (G. Zeimann et al., 2023, in preparation). Additional support is also provided by the Dark Energy Explorers²⁴ citizen science project (L. House et al., 2023, in preparation).

For this work, we select the 51,863 HPSC-1 spectra from objects classified as $1.88 < z < 3.52$ galaxies, explicitly excluding objects containing AGNs, as identified by ELiXer or Liu et al. 2022 (see also Section 4.1). The redshift range is defined by where Ly α falls within the HETDEX spectral bandpass. The AGN classifications made by ELiXer within this redshift range are based on (i) the detection of Ly α found with other emission-lines combinations consistent with AGNs, such as C III], C IV, He II, etc., (ii) broad Ly α emission $\gtrsim 1200$ km s $^{-1}$, or (iii) a position and photometric magnitude match to an object from an external catalog that is classified as an AGN. More exhaustive AGN classifications are made by Liu et al. (2022) based on single emission line and line pair matching with enhanced, multi-Gaussian fitting, the continuum profile, and visual inspection of all candidate AGN HETDEX spectra along with archival photometry.

3. Methods

The details on the HETDEX data pipeline, including calibrations, sky subtraction, and spectra extraction, can be found in Gebhardt et al. (2021). The creation and general description of the public data catalog release, HPSC-1, is described in Mentuch Cooper et al. (2023). All galaxy spectra used in this work come from the aperture extracted, wavelength-rectified, PSF-weighted, atmospheric dispersion corrected, Milky Way dust dereddened data presented in HPSC-1. The additional corrections and operations applied to those spectra are described in the subsections that follow.

3.1. Sky Subtraction

Though the sky subtraction methodology is described in detail in Gebhardt et al. (2021), because of its direct relevance to several topics in this work, we present a brief overview of the salient points. The goal of the sky subtraction is to remove background light while preserving the light from astronomical sources. The background light comes from the atmosphere (literally, the “sky”), as well as instrumental effects such as thermal noise and scattered light in the optics. Furthermore, any large diffuse astrophysical source will be included in the sky background; for example, light from unresolved faint foreground and background galaxies that are uniformly distributed in the sky will add to the estimate of the background. There are additional complications discussed in Gebhardt et al. (2021) such as wavelength distortion in the spectrographs that can lead to sky background residuals.

Here we make use only of the local form of the HETDEX sky subtraction, as it is more stable than the full field sky subtraction in the pipeline version used to create HPSC-1, the source of the spectra for this work. The on-sky size of the local sky is $50'' \times 12''$, whereas the full sky is derived from the entire $21'$ diameter focal plane. While both sky subtractions use similar methods, the local sky subtraction employs 112 fibers for each amplifier (4 per IFU), and the full field sky subtraction uses all fibers in an exposure ($\sim 35,000$). The full sky

necessitates additional adjustments for amplifier-to-amplifier variations and other complications. For emission-line source detection, we rely on the local sky since it is more robust to instrumental effects and generates smaller background residuals.

For the local sky subtraction, fibers containing obvious continua are removed, including those with counts more than $3 \times$ the biweight scale of the fibers on the amplifier. The remaining fibers are then used to compute the per wavelength bin background from their biweight locations. Typically, 70%–80% of the fibers in an amplifier are used for this calculation, though it can be as low as 25%–30% when there is a star or other bright object in or near the field of view of the amplifier. As HETDEX detections can include fibers from more than one amplifier, due to their size and/or their position within an IFU, the fibers included in their detection aperture can have different local sky subtraction corrections. One potential consequence of the local sky subtraction, which we revisit later, is that it can partly remove low-level flux actually associated with detected galaxies if that flux is spatially extended over a large portion of an IFU.

3.2. Sky Subtraction Residual

Similar to the background residual correction presented in Davis et al. (2021), the LAE spectra stacked in this work have an observed-frame residual correction applied prior to their shift to the rest frame. The purpose of this correction is to account for small systematics in the calibration, and the average extra light in the extraction apertures that come from faint, undetected background and foreground sources that are undetectable at the individual detection level. In Davis et al. (2021), apparently empty individual *sky fibers* are selected, sorted, and stacked on a per-observation basis and used to correct the individual fibers of the LAE detection from the matched observation. However, in this work, given the large number of statistics of the $250 \times$ larger LAE sample, we select entire apertures rather than individual fibers and average over many observations instead of applying separate corrections for each observation.

Using the observations from 2018 June, when the IFU array became significantly populated, through June 2020, the end of data acquisition for HPSC-1, we collect up to 200 spectra from random *empty* $3.''5$ radius apertures within each of the ~ 2000 observations in this range; this radius matches the size of the standard HETDEX aperture (Gebhardt et al. 2021), and the spectra are extracted using the same method as the normal HETDEX detections. The center of each aperture is randomly selected from the footprint of the observation’s IFU coverage with the following constraints:

1. No aperture center can be within $1.''5$ of another. This means the apertures can overlap but not near their central regions where the PSF weights are highest.
2. There must be at least 15 fibers included in the aperture over the three exposures comprising the observation. This avoids apertures where a significant portion falls off the edge of an IFU.
3. The measured g magnitude in the PSF-weighted spectra extracted under the aperture must be fainter than 24, and have a median flux density between 3900 and 5400 Å greater than -4×10^{-18} erg s $^{-1}$ cm $^{-2}$ Å $^{-1}$. This satisfies the empty requirement, given that the

²⁴ <https://www.zooniverse.org/projects/erinmc/dark-energy-explorers>

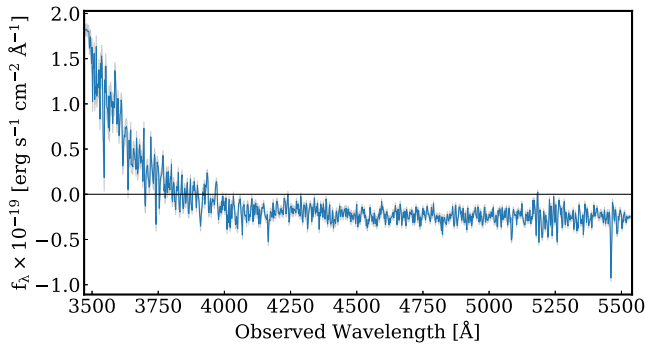


Figure 1. Weighted biweight average of the residuals produced by sky subtraction derived from stacking more than 300,000 random, empty $3''$ radius apertures taken from HPSC-1 HETDEX observations. The errors are shown in gray and are derived via σ_b/\sqrt{N} where σ_b is the biweight scale. The f_λ level of this residual spectrum is $\sim 1\%$ of the HETDEX flux limits (Gebhardt et al. 2021), and thus, meaningful only when stacking large numbers of spectra. The rise in the far blue end of the spectrum is primarily due to a limitation in the instrument and the slightly negative flux redward of ~ 4000 Å is a result of a small overcorrection in the sky subtraction. The spectrum is available in electronic form.

(The data used to create this figure are available.)

HETDEX depth is close to 25 in g in good conditions but can be near 24 in poor seeing (Gebhardt et al. 2021; Davis et al. 2023; Mentuch Cooper et al. 2023). The negative lower limit accounts for the possibility of some over-subtraction and for excursions due to noise.

4. There can be no detected emission lines within the extracted spectrum and no HETDEX detections within $2''$.

These criteria yield more than 300,000 PSF-weighted spectra (not all observations yield the target 200 empty apertures) that are stacked along their native HETDEX 2 Å wavelength bins using the biweight measure of central location (Beers et al. 1990) using the same method described in Davis et al. 2021. The result is shown in Figure 1 with the residual spectrum flux in blue and the flux uncertainties for each wavelength bin in gray. The reported uncertainties are statistical and are defined as σ_b/\sqrt{N} , where σ_b is the biweight scale of the N contributing empty aperture measured spectra for that wavelength bin. The spectrum is also made available in electronic form. Sky subtraction residual spectra created by stacking under alternate subselections of the full $\sim 300,000$ sample are stable with respect to variations in the seeing FWHM, throughput and instrument response, date, and observed decl.

Each LAE spectrum is corrected by subtracting this sky subtraction residual in its observed frame. For individual spectra the correction is less than 1%, far below the noise level; the systematic becomes meaningful only when stacking hundreds or thousands of galaxy spectra. Figure 1 shows a distinct rise in the far blue caused by instrumental limitations and is slightly negative redward of about 4000 Å, indicating a small over-subtraction by the reduction pipeline. Both these effects are more than 100× smaller than the typical HETDEX flux limits ($\sim 2 \times 10^{-17}$ erg s $^{-1}$ cm $^{-2}$ Å $^{-1}$, but can rise up to 10× higher blueward of 3800 Å; Gebhardt et al. 2021) and are inconsequential for individual spectra. They only become significant when stacking large numbers of spectra. Future data releases will include improvements in the data-reduction pipeline to better address these issues.

3.3. Shift to the Rest Frame

As described in the previous subsection, the spectra are first corrected for the sky subtraction residual in their observed frame. Depending on the needs of the analysis, all spectra are corrected for wavelength- and redshift-dependent fractional IGM transmission. The IGM correction applied in this work is from CIGALE (Boquien et al. 2019), which is derived from Meiksin 2006. The individual application of the IGM transmission correction can be highly uncertain since IGM attenuation is dependent on the particular sight line (Inoue et al. 2014). However, since we are averaging over many thousands of spectra, this becomes naturally statistical (Dijkstra et al. 2007; Zheng et al. 2010; Laursen et al. 2011; Behrens et al. 2018; Steidel et al. 2018; Gurung-López et al. 2019; Byrohl & Gronke 2020). Lastly, the spectra are shifted to their own rest frame so that they can be aligned for stacking.

The rest-frame shift has two components, one for the wavelength bins and one for the flux density at each bin center. Since the reported HETDEX wavelengths are in air, the observed wavelengths are converted to vacuum (Greisen et al. 2006) and then simply adjusted by $(1+z)$ where z is determined from the Gaussian-fitted line center of the Ly α emission line (Mentuch Cooper et al. 2023). As discussed in Davis et al. 2021 and later in this work (Section 4.3), there is no correction applied for any Ly α velocity offset from an individual galaxy's systemic redshift. Depending on the science needs, this wavelength-only shift, by itself, may be sufficient, but it only represents the observed flux at rest wavelengths: when stacking, this can create a bias against higher redshift objects due to increased cosmological dimming. For this work, and to counteract this bias, we also convert the observed flux density (f_λ) to a luminosity density (L_λ or L_ν , as needed). Please note that here we use *luminosity density* as an analog to flux density, not as a luminosity per unit volume. This conversion is a straightforward application of

$$L_\lambda = 4\pi D_L^2 f_\lambda (1+z), \quad (1)$$

where D_L is the luminosity distance. Where L_ν is needed, we simply multiply L_λ by λ^2/c . Unless stated otherwise, z (specifically, $1+z$) is defined as the ratio of the observed frame, vacuum-shifted, Gaussian-fitted emission-line center wavelength to the vacuum rest-frame wavelength.

3.4. Stacking

Once the previously described corrections and shifts are made, the spectra are stacked using the same method described in Davis et al. (2021). The rest-frame wavelength spacing is adopted from the highest redshift object to be stacked, with the blue and red wavelength endpoints coming from the highest and lowest redshift objects, respectively. All spectra are then linearly interpolated onto this wavelength grid and stacked in each wavelength bin using the weighted biweight statistic (Davis et al. 2021), as a modification of the biweight statistic described in Beers et al. (1990). The weighted biweight alters the biweight location slightly by including an additional weight for each element in the sample. The weight used in the stack is the inverse of the uncertainty on the flux measures within each wavelength bin, such that the more uncertain fluxes have a reduced contribution to the biweight location. We note that for these large data sets ($\gg 10^4$ spectra), the biweight and weighted biweight perform very similarly to a median average, with a

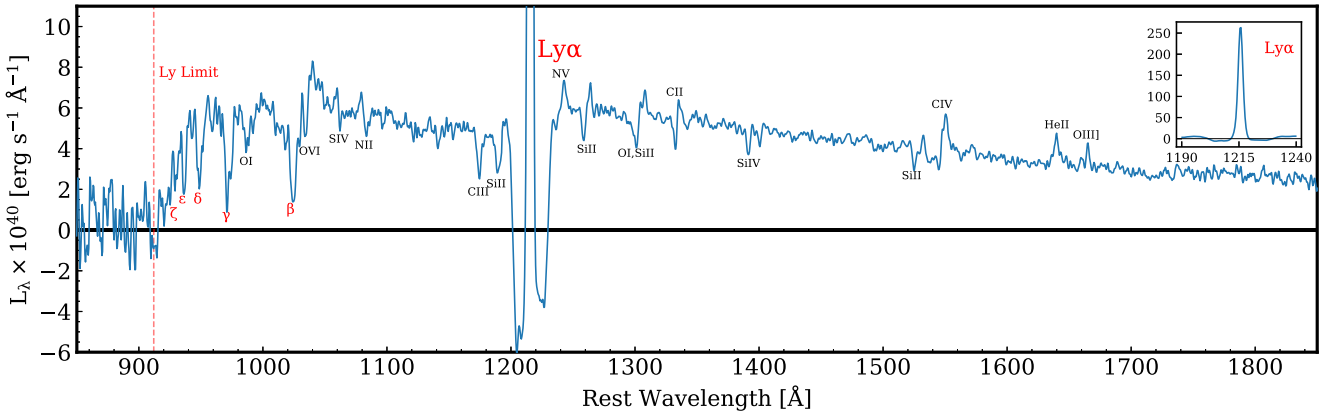


Figure 2. Rest-frame weighted biweight-averaged stack of $\sim 50,000$ LAEs from HPSC-1 between $1.9 < z < 3.5$ (not corrected for IGM transmission). The spectrum has been smoothed with a 1 pixel (0.44 \AA) Gaussian kernel (σ). As noted in Section 3.4, the number of contributing galaxies (Figure 3 green curve, bottom panel) decreases with distance from Ly α , dropping to 16% in the extreme blue and 4% in the red. The uncertainties (Figure 3 orange curve, top panel) are $\sim 5\%$ except for near edges of the wavelength range where they rise to $\sim 25\%$ at the red end and $\sim 100\%$ in the far blue. Despite containing more contributing spectra, the blue end of the spectrum has larger uncertainties due to the performance of the CCD (Gebhardt et al. 2021). These uncertainties are defined as $\sigma_b/\sqrt{n_\lambda}$ where σ_b is the biweight scale and n_λ is the number of spectra contributing to the wavelength bin. The inset in the upper right shows the full height of the Ly α line in the same luminosity units. The deep troughs near the Ly α line have some physical motivation, but are artificially enhanced by the data-reduction pipeline (see Section 4.4). This spectrum, with the associated error array, is available in electronic form.

(The data used to create this figure are available.)

brief comparison of the two methods provided in Section 4. In all cases, the default tuning constants are used. For the biweight location (or weighted biweight location), the constant is 6 and for the biweight scale it is 9.

While it is common practice to normalize the spectra before stacking, often to the flux near 1500 \AA for LBGs and LAEs, (Vargas et al. 2014; Marchi et al. 2017; Steidel et al. 2018, and others), the nature of the HETDEX data makes this impractical. For the vast majority of the spectra presented in this work, only the Ly α emission is detectable above the flux limits, so there is no measured continuum against which to normalize. Instead, we stack the un-normalized spectra first, and then, where appropriate for the analysis, we normalize the stack against the flux over a section of its wavelengths.

Since the HETDEX wavelength window is fixed at $3500\text{--}5500 \text{ \AA}$ and the LAEs span $1.9 < z < 3.5$ (Gebhardt et al. 2021), only the wavelength region immediately around rest-frame Ly α can receive contributions from all spectra (the number of contributing spectra for each wavelength bin is included as a column in the stacked spectrum data file). The fluxes in wavelength bins increasingly blueward of Ly α are populated by LAEs at increasingly higher redshifts, while the opposite is true moving redward of Ly α .

4. Results

The stack of the full $50,000$ $1.9 < z < 3.5$ LAEs (median $z = 2.55$), not corrected for IGM transmission, is presented in Figure 2 in terms of L_λ normalized to the median between 1475 and 1525 \AA (L_{1500}). The data for this figure, including the number of contributing spectra and uncertainties for each wavelength bin, is available in electronic form.

The Ly α emission-line fitting is performed with ELiXer (Davis et al. 2023) and the S/N has increased from a median of 6 for the individual galaxies in the sample to near 1000 in the stack. The uncertainties on the stack (shown as the orange curve in the top panel of Figure 3 as absolute uncertainties) are $\sim 5\%$, except near the wavelengths farthest from Ly α , where

they grow to $\gtrsim 25\%$ in the far red and spike above 100% in the far blue. The latter effect is due to the declining CCD sensitivity in the blue (Gebhardt et al. 2021) and the decreasing number of contributing objects (shown as the green curve in the bottom panel of Figure 3) at the spectral extremes (16% of the maximum in the far blue and 4% in the far red). These uncertainties are defined as standard errors with $\sigma_b/\sqrt{n_\lambda}$, where σ_b is the biweight scale and n_λ is the number of spectra contributing to the wavelength bin centered on λ . Figure 4 compares the stack to a typical HPSC-1 LAE (ID: 2100541366; R.A., decl.: $150.127594 + 2.295267$), selected for the similarity of its properties ($z = 2.566$, $g = 25.3$, Ly α S/N = 5.9, Ly α log luminosity = 42.81 (erg s^{-1}), and $W_\lambda(\text{Ly}\alpha) = 87 \text{ \AA}$) to the ensemble and sample averages. The figure illustrates the S/N improvements gained through stacking. Using wavelengths redward of Ly α ($1250\text{--}1650 \text{ \AA}$, rest) and defining the S/N simply as the mean flux divided by the mean (analogous) error on that flux (Gebhardt et al. 2021) and the standard error-like definition above, there is an increase of more than $300\times$ from the mean S/N ≈ 0.06 for the continuum in an individual detection to the mean S/N ≈ 21 in the stack.

As noted earlier, the differences between the biweight and median methods are small for large sample sizes. For the spectra in this work, the median of the differences between stacks using the biweight method (Section 3.4 and Figure 2) and using a median is 2.6%, measured from rest frame $850\text{--}1850 \text{ \AA}$, or 3.1% over the entire wavelength range, $768\text{--}1918 \text{ \AA}$. For the same stacks, the biweight location of the differences is nearly identical to the median differences at 2.6% and 3.0% for the same two wavelength ranges. Here we define the difference per wavelength bin as

$$\frac{|L_\lambda^b - L_\lambda^m|}{\frac{1}{2}(L_\lambda^b + L_\lambda^m)}, \quad (2)$$

where L_λ^b is the luminosity in wavelength bins from the biweight-averaged stack and L_λ^m is the luminosity in the same wavelength bins from the median-average stack (see the

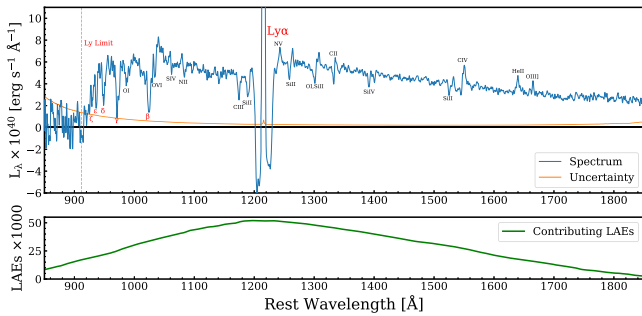


Figure 3. Rest-frame weighted biweight-averaged stack of $\sim 50,000$ LAEs from HPSC-1 between $1.9 < z < 3.5$ (not corrected for IGM transmission), as in Figure 2, with the uncertainty shown in orange (top panel) and the number of contributing galaxies per wavelength bin in green (bottom panel).

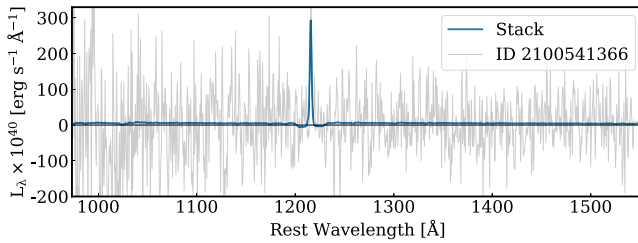


Figure 4. Stack from Figure 2 compared to a typical HPSC-1 LAE, ID: 2100541366 (R.A., decl.: $150.127594 + 2.295267$) to illustrate the S/N gains. This LAE is selected as it has properties similar to the sample average and ensemble: $z = 2.566$, $g = 25.3$, $\text{Ly}\alpha \text{ S/N} = 5.9$, $\text{Ly}\alpha \log \text{Luminosity} = 42.81$ (erg s^{-1}), $W_\lambda(\text{Ly}\alpha) = 87 \text{ \AA}$. The figure is cropped to the rest-frame wavelengths covered by the individual detection and aligned at $\text{Ly}\alpha$. If we define the S/N simply as the ratio of the means of the flux and the errors on that flux (Gebhardt et al. 2021, and Section 4 in this work) between 1250 and 1650 \AA , we see an improvement of more than $300\times$ from the continuum S/N ≈ 0.06 in the individual detection to the S/N ≈ 21 in the stack.

Methods section, Section 3) for the details on the stacking processes). For Gaussian distributions, the biweight location and median differ by $\ll 1\%$ and the standard deviation, σ , and the biweight scale, σ_b , by $< 1\%$.

Selected features of the stack (Figure 2) are discussed and interpreted, quantitatively and qualitatively, in subsequent subsections.

4.1. Caveats

Before proceeding further, it is necessary to acknowledge several caveats that can affect the analyses and interpretations.

Contamination of the sample of HPSC-1 LAEs by misclassified emission, in particular that of [O II], is quite low at an estimated value of $\sim 2.5\%-3.0\%$ (Mentuch Cooper et al. 2023). However, since it is not zero, it may slightly dilute the signal of the underlying continuum. Another $0.5\%-2.0\%$ of contamination could come from other individually detected lines such as C III], C IV, or Mg II, some of which are associated with possible AGNs. And though we make efforts to exclude AGNs through the identification of broad-line ($> 1200 \text{ km s}^{-1}$) pairs (e.g., Ly α + C IV, C IV+ C III], O VI+ Ly α , etc.), emission-line profile fitting, catalog matching, and visual inspection (Liu et al. 2022; Davis et al. 2023), some AGNs (particularly single narrow-line Type II AGNs and some broad-line objects where a second line is not identified by the pipeline) may remain in the LAE sample (Liu et al. 2022; Lujan Niemeyer et al. 2022; Davis et al. 2023; Mentuch Cooper et al. 2023). Some fraction of the detections, particularly at lower

emission-line S/N, may also be false detections of noise. While work is ongoing to better quantify the specific rates of these false detections, for the LAEs of HPSC-1, as described in Section 6.6 of Mentuch Cooper et al. (2023) positively confirm that 91% of the detections in a subsample of LAEs with repeat observations and thus sets an upper limit of 9% on the total fraction of contaminants.

Unlike Davis et al. (2021), the spectra in the stack have not been selected to exclude LAEs with nearby neighbors, as that information is absent from this data release. Similarly, the spectra have not been deblended to remove the contribution of flux by neighboring objects (D. Davis et al. 2023, in preparation). While the removal of the sky subtraction residual should largely handle the average contribution of faint line-of-sight interlopers, excess flux from these sky-adjacent neighbors can still be present in the individual galaxy spectra and find its way into the stacks.

While the HETDEX catalog has no galaxy preselection, its emission-line detections are flux limited ($\sim 4 \times 10^{-17} \text{ erg s}^{-1} \text{ cm}^{-2}$; Gebhardt et al. 2021), and the HPSC-1 catalog excludes detections with emission-line S/N < 5.5 (Mentuch Cooper et al. 2023). There is thus a bias against detecting galaxies with observationally fainter Ly α , which necessarily increases with increasing redshift. However, the use of the median-like weighted biweight mechanics (Beers et al. 1990; Davis et al. 2021) in the stack does mitigate the influence of bright outliers, which helps maintain the representative nature of the stack.

As previously stated and further discussed in Section 4.3, the spectra are aligned for stacking based on their Gaussian-fitted Ly α line. This can lead to a $\sim 1 \text{ \AA}$ smearing of spectral features due to the individual Ly α redshift offsets from the galaxies' systemic redshifts.

Lastly, as noted in Section 3.4, the wavelength regions farther from Ly α have fewer contributing spectra and thus increased uncertainty in the stack compared to wavelengths closer to the Ly α line. Furthermore, we have to assume that evolution in the galaxies over those redshift ranges of each stack is minor, in order to consider the stacked spectrum, as a whole, as representative of the underlying sample.

4.2. Representative Stack

Table 1 presents a summary of several properties (see the table note for descriptions) of the full data set and full stack along with three additional subselections that divide the sample by redshift. The redshift distribution, with mean $z = 2.6$, for this work is shown in Figure 5. Additional binnings based on other properties will be presented in future works. With the exception of the average r magnitude, which is included from various archival photometric imaging catalogs that overlap the HETDEX observations (Davis et al. 2021, 2023), the properties are measured from the individual spectra or the stacked spectra. A comparison of the biweight location (\tilde{x}_b) values of g , Ly α Luminosity, and Ly α equivalent width to the values derived from the stacked spectra demonstrates that they agree very well, suggesting the stacks are, indeed, similar to an average representation of the samples. We acknowledge that both the biweights of g and $W_\lambda(\text{Ly}\alpha)$ are more limited comparisons as HETDEX cannot measure continuum magnitudes fainter than ~ 25 in g ; hence, $W_\lambda(\text{Ly}\alpha)$ is a lower limit (Gebhardt et al. 2021; Davis et al. 2023; Mentuch Cooper et al. 2023).

Table 1
Summary of Ensemble Properties by Redshift Range

Redshift (1)	N (2)	$\langle g \rangle$ (3)	Stack g (4)	$\langle r \rangle$ (5)	$\langle L_{\text{Ly}\alpha} \rangle$ (6)	Stack $L_{\text{Ly}\alpha}$ (7)	$\langle W_{\lambda}(\text{Ly}\alpha) \rangle$ (8)	Stack $W_{\lambda}(\text{Ly}\alpha)$ (9)
$1.9 < z < 3.5$	52,000	$\tilde{x}_b = 25.9, \sigma_b = 1.30$	25.6	$\tilde{x}_b = 25.5, \sigma_b = 1.16$	$\tilde{x}_b = 42.92, \sigma_b = 0.212$	42.83	$\tilde{x}_b = 93.1, \sigma_b = 84.0$	114.0
$2.0 < z < 2.5$	21,000	$\tilde{x}_b = 25.8, \sigma_b = 1.35$	25.3	$\tilde{x}_b = 25.3, \sigma_b = 1.21$	$\tilde{x}_b = 42.86, \sigma_b = 0.211$	42.77	$\tilde{x}_b = 89.9, \sigma_b = 86.5$	108.8
$2.5 < z < 3.0$	18,000	$\tilde{x}_b = 25.8, \sigma_b = 1.27$	25.6	$\tilde{x}_b = 25.4, \sigma_b = 1.12$	$\tilde{x}_b = 42.91, \sigma_b = 0.187$	42.84	$\tilde{x}_b = 80.9, \sigma_b = 72.6$	101.7
$3.0 < z < 3.5$	11,000	$\tilde{x}_b = 26.2, \sigma_b = 1.18$	26.2	$\tilde{x}_b = 26.0, \sigma_b = 0.83$	$\tilde{x}_b = 43.03, \sigma_b = 0.180$	42.96	$\tilde{x}_b = 107, \sigma_b = 81.4$	130.0

Notes. (1) Redshift range of (sub)selection. (2) Number of galaxies in the (sub)selection to the nearest 1000. (3) The biweight location (\tilde{x}_b) and biweight scale (σ_b) of the Sloan Digital Sky Survey (SDSS) g magnitude of individual LAE detections as computed from the HETDEX spectra using the *speclite* Python package (Kirkby et al. 2023; see also, Davis et al. 2023). Though always computed, values $\gtrsim 25$ are fainter than the HETDEX detection limit. (4) The SDSS g magnitude computed from the observed frame stack of HETDEX spectra, again using *speclite*. Given the high S/N of the stack, the formal error on the fit magnitude is < 0.01 . (5) The biweight location and biweight scale of the r magnitudes of individual LAE detections as computed from photometric imaging with r coverage. Depth is catalog dependent (Davis et al. 2023), with 75% of HPSC-1 $\gtrsim 26$. Nondetections in the imaging are included as their respective limits. (6) The \log_{10} of the biweight location and biweight scale of the luminosity (erg per second) of the $\text{Ly}\alpha$ line of the individual LAE detections. (7) The \log_{10} of the luminosity (in erg per second) of the Gaussian-fitted $\text{Ly}\alpha$ line of the stack. Given the high S/N, uncertainties on the fits are $\ll 1\%$. (8) The biweight location and biweight scale of the rest-frame equivalent width (Å) of $\text{Ly}\alpha$ in the individual LAE detections. Since the continuum is often undetected, this is a lower limit. (9) The rest-frame equivalent width (Å) of $\text{Ly}\alpha$ in the stack. Given the high S/N, the errors on the fit are < 0.05 Å.

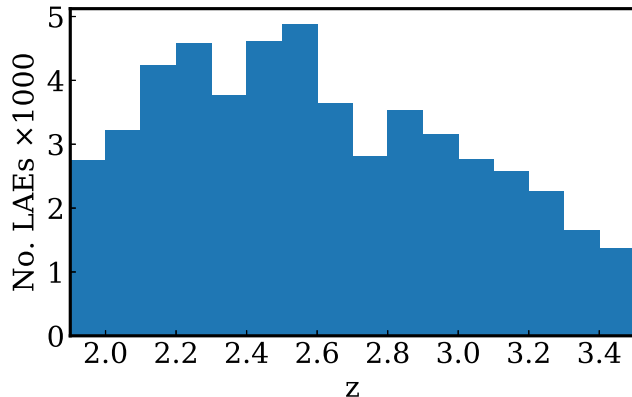


Figure 5. The redshift distribution (mean $z = 2.6$) of the $\sim 50,000$, flux-limited detection LAEs with $\text{Ly}\alpha$ S/N > 5.5 from HPSC-1.

4.3. $\text{Ly}\alpha$ Velocity Offset

Since we align the individual spectra based on their fitted, rest-frame $\text{Ly}\alpha$ emission-line centers, our figures show the stacked $\text{Ly}\alpha$ line centered at our adopted wavelength of 1215.67 \AA . However, due to the complexities of $\text{Ly}\alpha$ radiative transfer and the suppression of the flux near and just blueward of rest-frame $\text{Ly}\alpha$ (Verhamme et al. 2006; Smith et al. 2018; Verhamme et al. 2018; Byrohl & Gronke 2020, and many others), we are often fitting to the red peak of $\text{Ly}\alpha$, and there is an offset with respect to each galaxy’s systemic redshift. In the stack, this manifests as a slight offset between the expected and observed positions of the other emission and absorption features. Additionally, as the $\text{Ly}\alpha$ offset from systemic is variable by galaxy, there can also be a smearing/broadening of these other (stacked) spectral lines. With only $\text{Ly}\alpha$ detected in the vast majority of the HETDEX LAE spectra, and generally at $\text{S/N} \lesssim 6$ for HPSC-1, our ability to correct for the velocity offset of individual galaxies prior to stacking is limited (Davis et al. 2021). However, as we estimate the typical velocity offset to be at most a few hundred kilometers per second (see below), the impact on this work is small and we do not refine it further here.

To estimate the average $\text{Ly}\alpha$ velocity offset in our ensemble, we repeatedly fit the center lines of several emission and absorption features using a simple Markov Chain Monte Carlo (MCMC) Gaussian fitting code and compute a velocity offset from the assumed fiducial wavelength. These features are selected as they are clear, have high S/N, and are not significantly blended with any other lines (or can have the blended portion easily masked). The results are summarized in Table 2.

The velocity offsets from the features are similar, though there is some obvious scatter likely as a combination of interstellar medium (ISM) and IGM confusion, outflows, and other kinematics. The overall mean, $235 \pm 18 \text{ km s}^{-1}$, provides a good estimate of the $\text{Ly}\alpha$ velocity offset for stack and thus for the typical HPSC-1 LAE. Where stated for the remainder of this work, we adopt a rounded value of 250 km s^{-1} for the velocity offset from systemic for the stack. Though LAEs can exhibit a sizeable difference in individual $\text{Ly}\alpha$ velocity offsets, this average is consistent with those of LAEs and LBGs found in Shapley et al. (2003, $\sim 360 \text{ km s}^{-1}$), Erb et al. (2014, $\sim 240 \text{ km s}^{-1}$), Shibuya et al. (2014, $\sim 230 \text{ km s}^{-1}$), Steidel et al. (2018, $\sim 300 \text{ km s}^{-1}$), and Muzahid et al. (2020, $\sim 170 \text{ km s}^{-1}$). A more

Table 2
 $\text{Ly}\alpha$ Velocity Offsets

Line	Fiducial $\lambda (\text{\AA})$	Offset (km s^{-1})
$\text{Ly}\beta^a$	1025.72	320 ± 58
C III	1175.71	330 ± 37
C IV ^b	1549.48	199 ± 27
He II ^c	1640.42	125 ± 41
O III ^d	1666.15	198 ± 28
Mean	NA	235 ± 18

Notes. Velocity offsets of various spectral lines from the $\text{Ly}\alpha$ aligned HPSC-1 stack (Figure 2) as measured against the MCMC Gaussian-fitted line centers. The last row is a simple, unweighted mean. Scatter is likely due to a combination of ISM and IGM confusion, outflows, and other kinematics.

^a Subject to ISM and IGM confusion.

^b Doublet; λ as unweighted mean.

^c Shows stellar (broad) and nebular (narrow) components.

^d Doublet; using the red peak only.

rigorous investigation is presented in L. Weiss et al. (2023, in preparation).

These estimates generally agree with and bracket the $\sim 200 \text{ km s}^{-1}$ reported for the much smaller, $z > 3$ sample in Davis et al. (2021). This equates to a less than 1 \AA offset in the adopted Lyman continuum region, $880\text{--}910 \text{ \AA}$. That work finds no significant impact on the Lyman continuum estimate measured over 30 \AA and no apparent change when applying a correction such as that in Verhamme et al. (2018), Byrohl et al. (2019), and Gurung-López et al. (2020). This small velocity offset is also consistent with the expectation of enhanced Lyman continuum leakage (Izotov et al. 2018; Naidu et al. 2021).

4.4. $\text{Ly}\alpha$ Troughs

On either side of the $\text{Ly}\alpha$ emission line, there are deep, negative *troughs*. While absorption is expected near the $\text{Ly}\alpha$ emission, the depths of the troughs, as shown in Figure 2, are enhanced by our reductions. Though scattering of photons near $\text{Ly}\alpha$ resonance by the H I in and around the LAEs is expected, the majority of the depths of these troughs are a result of the HETDEX sky subtraction and reduction pipeline (Section 3.1). The sky subtraction assumes that the sky off-source is the same as the sky on-source. Any differences in this assumption could then create a feature in the resulting stacked spectra. As one possible scenario, the version of the pipeline in this data release could over-subtract faint $\text{Ly}\alpha$ emission from halos around the LAEs that extend ~ 10 or more arcseconds. In this case, we could create a self-subtraction of the $\text{Ly}\alpha$ emission and cause the troughs to go negative. Another possible scenario is that a diffuse UV background exists as part of the general sky background we measure. In this case, the on-source sky could be different than the off-source sky due to absorption around $\text{Ly}\alpha$. A more complete discussion of the artificial troughs and real $\text{Ly}\alpha$ scattering is presented in L. Weiss et al. (2023, in preparation). For the measurements of this work, we simply avoid the $\text{Ly}\alpha$ troughs by masking them.

4.5. $\text{Ly}\alpha$ Luminosity

The calculations of the $\text{Ly}\alpha$ luminosity for both individual galaxy spectra and the stack are similar. For an individual galaxy, the identified $\text{Ly}\alpha$ emission line is fit with a simple Gaussian (Davis et al. 2023) whose area is the integrated flux, noting that the continuum level is a free parameter and allowed

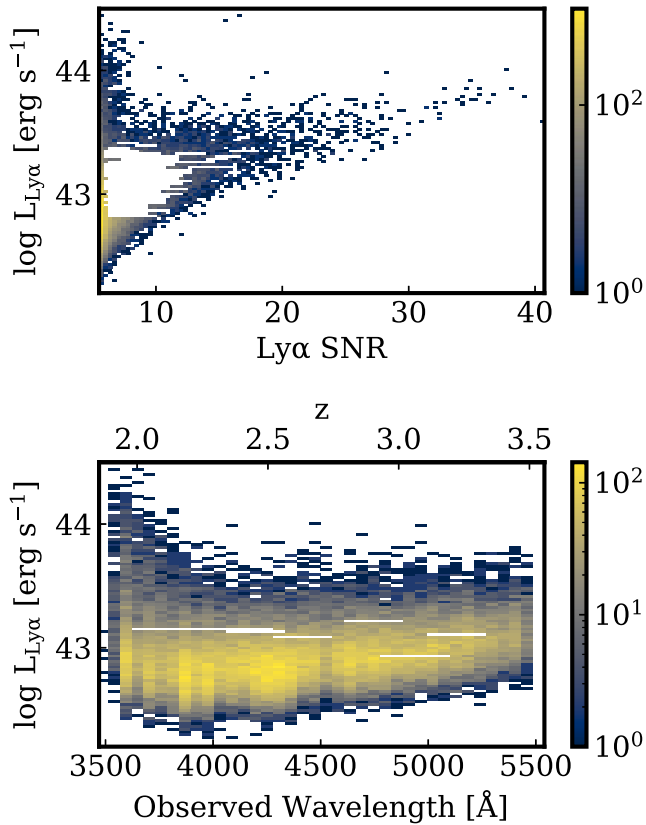


Figure 6. Ly α luminosity in the HPSC-1 as functions of Ly α S/N and observed wavelength. The color, independently for each panel, tracks the number of galaxies. The highest luminosities occur at the lowest S/N and bluest wavelengths where the diminishing throughput of the instrument amplifies the scatter intrinsic to low S/N detections. The lower figure also shows a trend to larger luminosities with longer wavelengths; this is due to the HETDEX flux limits (Gebhardt et al. 2021) and is consistent with cosmological dimming.

to be negative. That flux is then converted to a luminosity using Equation (1), but without the tailing $(1+z)$ term. For the L_λ stacked spectra, since we are already in the rest frame and in luminosity density, we simply fit a Gaussian where the continuum is set by the L_λ redward of Ly α and whose area is the integrated line luminosity with the Ly α trough regions (Section 4.4) masked out. This is the observed luminosity of the escaping Ly α . There are no additional corrections applied for extinction or attenuation by the rest-frame dust and ISM.

As shown in Table 1 and Figure 6, the individual galaxy Ly α log luminosities (i.e., $\log_{10}(L_{\text{Ly}\alpha}/[\text{erg s}^{-1}])$) in this sample range from 42.26–44.45 with a biweight location of 42.92 ± 0.212 and 1.9% of the Ly α emission lines greater than 43.50. At the brighter end, it is probable that some of the galaxies host unidentified AGNs and some luminosities may be inflated due to measurement uncertainty. The full sample-stacked spectra have a Ly α luminosity of 42.83, about 20% lower than the sample biweight, though well within the uncertainty. The fit to the Ly α line of the stack is a more precise average of the sample as a whole due to the increased S/N, since the continuum level is a free parameter for both the stack and the individual detections. The stacked continuum is well detected where continuum is rarely detected in individual HETDEX LAEs and the greatest spread in luminosities in the sample is associated with the lowest Ly α S/N detections, which represent the largest fraction of the sample (Figure 6).

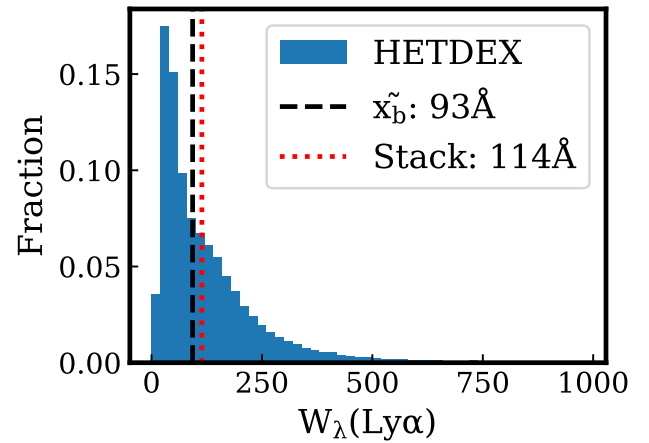


Figure 7. Distribution of Ly α rest-frame equivalent widths in HPSC-1. The y-axis is normalized to the full 50,000 LAEs of this work. The black dashed vertical line marks the biweight location value of the distribution and the red dotted line the value as computed from the stack of the spectra. As most LAEs in HPSC-1 do not have detected continua, the individual equivalent widths are generally lower limits. The continuum in the stacked spectrum (Figure 2) is clearly detected and that computed equivalent width is more secure. See also Table 1.

Table 1 naively shows a weak trend of increasing Ly α luminosity with increasing redshift bin, which could indicate some small evolution with redshift (Ciardullo et al. 2011, for example). However, the decrease is consistent with the loss due to the HETDEX flux limits and cosmological dimming.

4.6. Ly α Equivalent Widths

The Ly α rest-frame equivalent widths, $W_\lambda(\text{Ly}\alpha)$, are not explicitly reported in HPSC-1 but are shown in Figure 7, along with the sample biweight location and the corresponding stack value. Each $W_\lambda(\text{Ly}\alpha)$ is computed from the integrated Ly α flux and a combined estimation of the continuum from the spectrum and associated photometry (Davis et al. 2023; Mentuch Cooper et al. 2023) divided by $(1+z)$. For each of the rest-frame stacked spectra (Table 1), $W_\lambda(\text{Ly}\alpha)$ is simply the ratio of the integrated Ly α luminosity to the fitted continuum around the Ly α line, again with the Ly α troughs masked. As with the Ly α luminosities, the stacked spectra measurement of $W_\lambda(\text{Ly}\alpha)$ is consistent with the biweight measure from the sample, but the stack may provide a more robust average as the continuum is detected; HETDEX rarely detects the continua of $z \gtrsim 1.9$ galaxies.

The HPSC-1 equivalent width distribution is similar to that found with MUSE in Kerutt et al. 2022. HPSC-1 reports that 15% of its LAEs have $W_\lambda(\text{Ly}\alpha) > 240 \text{ \AA}$ and the full sample has a biweight location value of $93.1 \pm 84.0 \text{ \AA}$; Kerutt et al. 2022 reports that 16% (in their full sample) of the galaxies have $W_\lambda(\text{Ly}\alpha) > 240 \text{ \AA}$ and the characteristic $W_\lambda(\text{Ly}\alpha)$ is 95.5 \AA . Restricting the comparison of the two samples to their LAEs within the overlapping redshift coverage, $2.9 < z < 3.5$, the distributions deviate a bit more, but remain similar, see Figure 8. The redshift-restricted MUSE sample of 591 LAEs (out of 1920 LAEs of the full sample) has 16% with $W_\lambda(\text{Ly}\alpha)$ above 240 \AA versus 11% for the redshift-restricted HPSC-1 sample of 13,500 LAEs. The biweight locations of the restricted MUSE $W_\lambda(\text{Ly}\alpha)$ and HPSC-1 samples are 85.4 and 102.7 \AA , respectively.

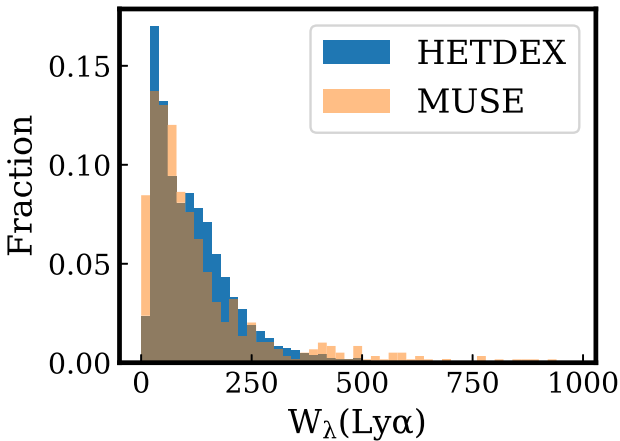


Figure 8. Normalized histograms of the 13,500 HPSC-1 LAEs in $2.9 < z < 3.5$ and the 591 MUSE LAEs of the same redshift range (Kerutt et al. 2022). The distributions are similar, with 11% of these HETDEX LAEs and 16% of the MUSE LAEs exhibiting estimated $W_\lambda(\text{Ly}\alpha)$ values $> 240 \text{ \AA}$ and with biweight locations of $W_\lambda(\text{Ly}\alpha)$ values of 102.7 ± 80.2 and $85.4 \pm 78.7 \text{ \AA}$, respectively.

The HPSC-1 equivalent widths given in Table 1 and Figure 9 might also suggest some weak evolution with redshift similar to findings in Ciardullo et al. 2011. However, this is even less clear with the HPSC-1 data than the possible trend with Ly α luminosity as the equivalent width measures are less secure due to the lack of detected continua and are also biased toward the detection of brighter Ly α at higher redshifts due to cosmological dimming.

4.7. UV Continuum Slope and UV Magnitude

The observed UV continuum slope, β , modeled as $f(\lambda) \propto \lambda^\beta$, is taken from the full stack (Figure 2) and measured from 1250–1850 \AA by fitting a simple least squares optimized power law after masking the features near 1260, 1302, 1335, 1394, 1549, 1640, and 1665 \AA . Given the wavelength range, this is similar to β_{18} in Calzetti 2001. The best-fit β , -2.36 ± 0.09 , implies that our average LAE has a young, low-metallicity stellar population, a large ionizing photon production efficiency, and very little dust extinction (Calzetti 2001; Bouwens et al. 2010b; Calabro et al. 2021; Chisholm et al. 2022; Saldana-Lopez et al. 2022). This is in line with that expected for the $z \sim 3$ LAE population (see also Section 4.9). This also suggests an increased likelihood of Lyman continuum escape and may indicate a recent (5–15 Myr) burst of star formation (Calzetti 2001; Calabro et al. 2021; Chisholm et al. 2022; Saldana-Lopez et al. 2022).

The absolute UV magnitude (M_{UV} or M_{1500}) of the full stack is computed from the mean and median luminosity density between 1400 and 1600 \AA in the rest frame, using the standard 3631 Jy AB magnitude zero-point scaled to $L_{\nu,0}$ of $4.3454 \times 10^{20} \text{ erg s}^{-1} \text{ Hz}^{-1}$ at 10 pc. The M_{UV} from the mean values corresponds to a medium bright galaxy with -19.67 ± 0.13 , while the median values are essentially identical, -19.68 ± 0.13 . The errors are statistical and come from the propagation of the standard deviation of the flux density between 1400 and 1600 \AA in the rest frame.

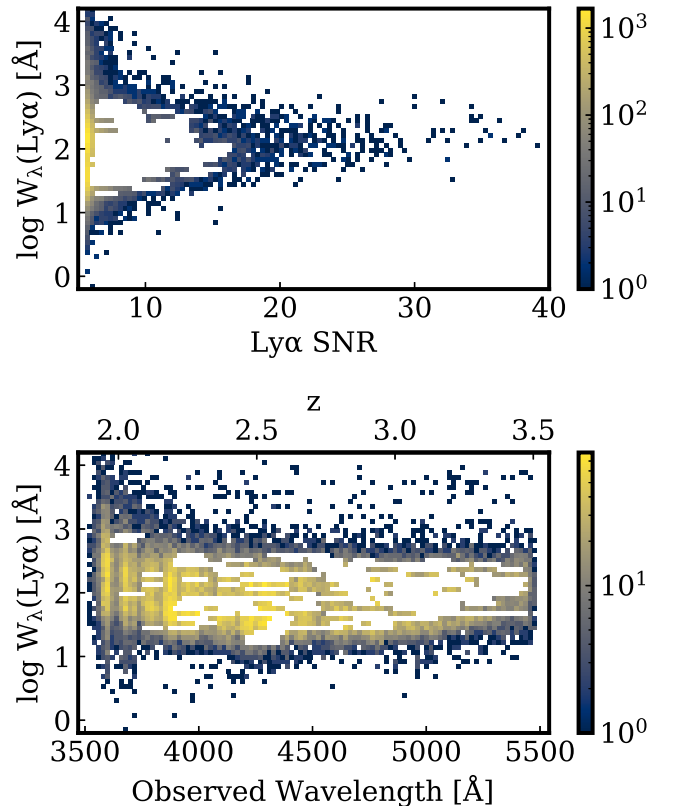


Figure 9. Ly α rest-frame equivalent widths in HPSC-1 as functions of Ly α S/N and observed wavelength. The color, independently for each panel, tracks the number of galaxies. Since most HPSC-1 spectra do not have a detectable continuum, the equivalent widths are lower limits. There is an obvious loss of lower $W_\lambda(\text{Ly}\alpha)$ objects with increasing redshift, which is likely just the result of the HETDEX flux limits and cosmological dimming. The evidence for a true increase in equivalent width with redshift in this data set is very weak at best. See also Table 1.

4.8. P Cygni Profiles

P Cygni line profiles (Beals 1934) are clearly visible in Figure 2, for example O VI (1032, 1038 \AA), N V (1241 \AA), and, to a lesser degree, C IV (1549 \AA). These profiles are complex combinations of nebular and stellar absorption and emission, and contain a wealth of information on the stellar population, star formation history, and the metal enrichment of the galaxy, but a proper decomposition and fitting is beyond the intended scope of this work. However, qualitatively speaking, the P Cygni profile is a telltale indicator of strong stellar winds, massive stars, and recent star formation (Steidel et al. 1996; Leitherer et al. 2001; Chisholm et al. 2019). While not exhibiting a P Cygni, the extremely broad He II (1640 \AA) emission, $940 \pm 130 \text{ km s}^{-1}$, is also strongly suggestive of a very young population (Chisholm et al. 2019). This is consistent with our picture of LAEs, and the clarity of the profile in the stack further highlights the S/N gains and additional physics that is not directly accessible in the individual HPSC-1 spectra.

4.9. Spectral Energy Distribution Fitting

To model and gain some understanding of the underlying stellar population, we perform spectral energy distribution (SED) fitting on the stacked spectrum (Figure 2). Since we are limited by the wavelength coverage in this spectrum to the rest-

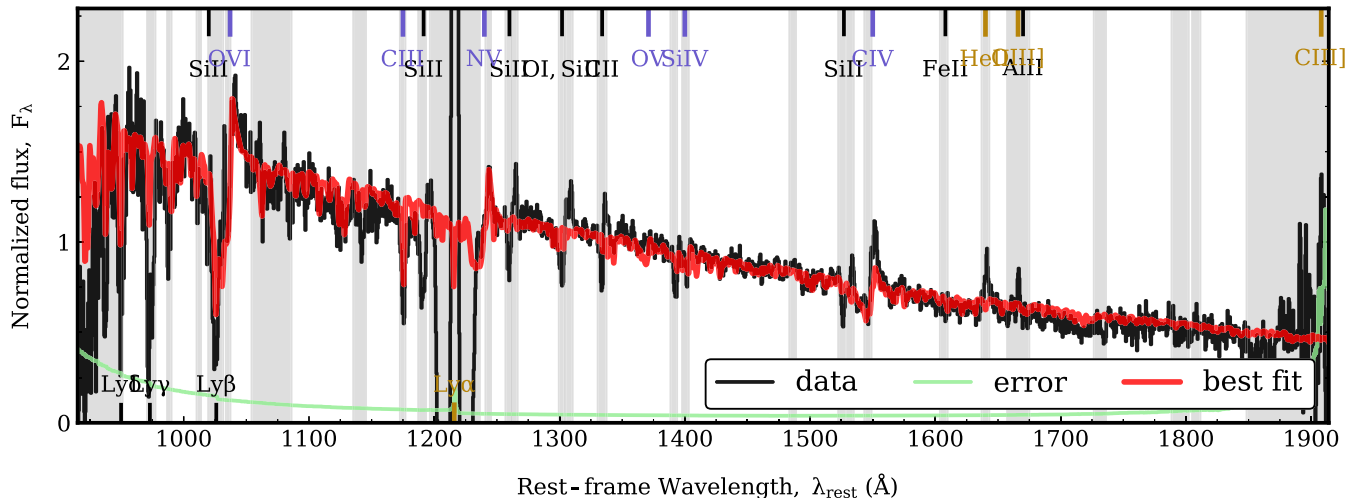


Figure 10. Best-fitting, lowest- χ^2 , FiCUS model (SB99 + SMC in Table 3). The black curve is the IGM corrected version of the full 50,000 stacked spectra shown in Figure 2 and the red curve denotes the FiCUS stellar continuum fit. Light gray regions, which correspond to most of the spectral features, are masked and not fit by the code. FiCUS is not designed to fit interstellar absorption or emission features.

Table 3
Summary of FiCUS SED Fitting

Model	χ^2	Age (Myr)	<5 Myr	$Z (Z_{\odot})$	$E(B - V)$	UV β	UV β^{int}
SB99 + R16	1.80	12.06 ± 1.41	0.75	0.26 ± 0.02	0.099 ± 0.002	-2.05 ± 0.01	-2.61 ± 0.01
SB99 + SMC	1.77	10.86 ± 1.41	0.75	0.28 ± 0.02	0.037 ± 0.001	-2.05 ± 0.01	-2.65 ± 0.01
BPASS + R16	1.80	15.68 ± 0.88	0.35	0.21 ± 0.02	0.078 ± 0.003	-2.10 ± 0.01	-2.54 ± 0.01
BPASS + SMC	1.78	14.79 ± 1.00	0.40	0.22 ± 0.02	0.030 ± 0.001	-2.07 ± 0.01	-2.57 ± 0.01

Notes. Results of four independent runs of the FiCUS stellar-continuum SED-fitting code (Section 4.9). Errors are statistical only. χ^2 is the goodness of fit to the HPSC-1 stacked spectrum (Figure 2). Age (Myr) is the model UV light-weighted average stellar age. <5 Myr is the fraction of the fitted stellar population younger than 5 Myr. Z is the model UV light-weighted average metallicity as a fraction of solar metallicity (Z_{\odot}). UV β is the UV continuum slope of the observed flux FiCUS model between 1250 and 1850 Å described in Section 4.7. UV β^{int} uses the same fitting but is applied to the FiCUS intrinsic flux model.

frame UV, we are only probing more recent star formation. The SED fitting is performed with the Python package for Fitting the stellar Continuum of UV Spectra or FiCUS²⁵ (Saldana-Lopez et al. 2022). Four separate runs use the Starburst99 (SB99; Leitherer et al. 2010) and the Binary Population and Spectral Synthesis (BPASS, v2.2.1; Eldridge et al. 2017) single-burst stellar population models, along with the dust attenuation models from (Reddy et al. 2016, hereafter R16) and the SMC extinction model by Prevot et al. (1984). All runs assume the same Kroupa (2001) initial mass function (IMF) with a $100 M_{\odot}$ upper limit and fit for 10 stellar ages (1, 2, 3, 4, 5, 8, 10, 15, 20, and 40 Myr) and four metallicities (5%, 20%, 40%, and 100% of Z_{\odot}). We use the IGM corrected version of the full stack spectrum (Figure 2) with an applied velocity offset of 250 km s⁻¹ (Section 4.3) and fit over 915–1915 Å in the rest frame, assuming a mean redshift of 2.604 for the 50,000 contributing galaxies. Key results of the four runs are summarized in Table 3 with the fit with the best χ^2 (row 2, SB99 + SMC) shown in Figure 10. We are not modeling Lyman continuum escape with FiCUS, as we are only fitting the continuum redward of the Lyman limit and are not yet confident using the restricted wavelength range for the $z > 3.0$ HETDEX LAEs where Lyman continuum could be observed.

While there are some small differences in the results from the four runs, with BPASS favoring slightly older, less enriched

stellar populations and the R16 dust model favoring slightly increased reddening, a consistent picture emerges of an ensemble-averaged galaxy with a young (10–15 Myr), metal-poor (0.2–0.3 Z_{\odot}) stellar population with minimal ($E(B - V)$ 0.03–0.10) reddening. The observed and intrinsic UV continuum slopes (ranging from $\beta = -2.10$ to -2.05 and -2.65 to -2.54 , respectively) for the four runs are fit over 1250–1850 Å as described in Section 4.7 and bracket the -2.36 UV continuum slope measured directly from the HPSC-1 stack. Saldana-Lopez et al. 2022, with support from Izotov et al. (2016), Salim et al. (2018), and Shvai et al. (2020), suggest that SB99 + SMC may best represent the conditions for these LAEs and, indeed, though perhaps coincidentally, that combination does produce the lowest χ^2 fit. This model (SB99 + SMC) does favor the youngest, UV light-weighted average stellar age with a significant fraction, just over 75%, of the light coming from stars with ages less than 5 Myr.

4.10. Relative Lyman Continuum Escape and Comparison to Reference Sample

For this measurement, we use L_{ν} instead of f_{ν} as explained in Section 3.4. We subselect the 11,000 HPSC-1 LAEs with $z > 3$, where the rest-frame Lyman continuum region, defined as (880–910 Å) for consistency with the literature (Shapley et al. 2006; Marchi et al. 2017; Steidel et al. 2018, and many others), falls within the HETDEX spectral range. The L_{900} value used is the weighted biweight location of the 68

²⁵ <https://github.com/asalda/FiCUS>

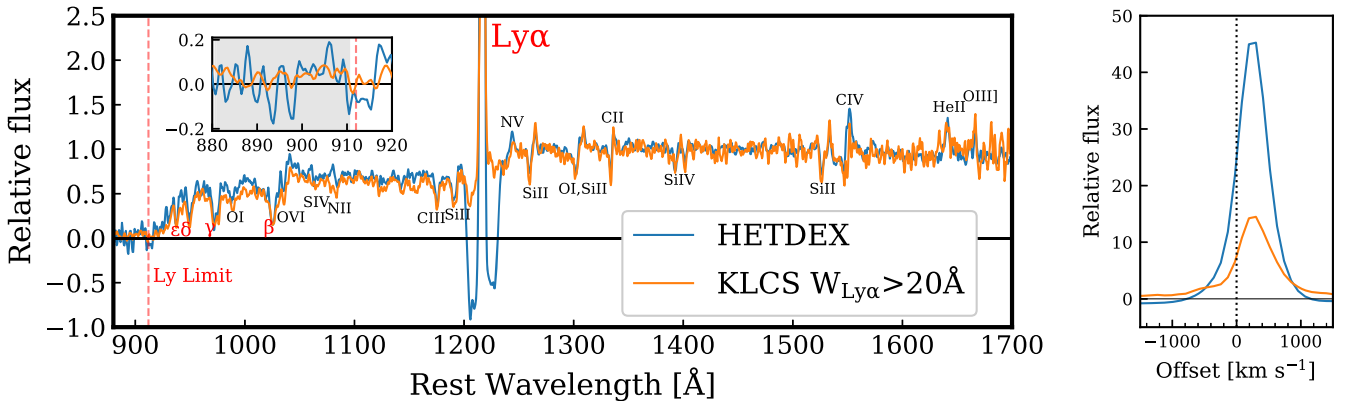


Figure 11. Comparison of the HETDEX (HPSC-1) rest frame stack to stack of the classical LAE subset (26 out of 124) of KLCS with $W_{\lambda}(\text{Ly}\alpha) > 20 \text{ \AA}$ (Steidel et al. 2018; Pahl et al. 2021). The HPSC-1 stack has been corrected for IGM transmission, shifted by 250 km s^{-1} (Section 4.3), and converted to L_{ν} units to match the KLCS data. Both spectra have been interpolated to the same wavelengths and smoothed with a 1 pixel (0.44 \AA) Gaussian kernel (σ). The left-hand panel shows a section of the UV rest frame. The zoom-in insert shows the Lyman continuum region (shaded). The right-hand panel shows a zoom around the $\text{Ly}\alpha$ lines in velocity space relative to the assumed systemic redshift.

wavelength bin luminosities in the residual subtracted (Section 3.2) and IGM transmission corrected (Boquien et al. 2019) L_{ν} spectrum between 880 and 910 \AA . The reported error is statistical; a standard error analog as the biweight scale of the same data divided by \sqrt{n} , where $n = 68$.

Since 1500 \AA is not available in the HETDEX spectral window for $z > 3$ galaxies, the L_{1500} value is estimated using two methods. The first estimate is based on a scaling of the weighted biweight flux density between 1268 and 1296 \AA using the slope fit between 1250 and 1525 \AA from our $2.6 < z < 3.5$ stack of 24,000 LAEs. That wider redshift range is selected as the narrowest window that includes sufficient wavelength coverage to the red of $\text{Ly}\alpha$ to capture the L_{1500} region. The L_{1500} normalized fitted slope is $5.11 (\pm 0.561) \times 10^{-4} L_{\nu} \text{ \AA}^{-1}$, and results in a stack average IGM corrected $L_{900}/L_{1500}(\text{out}) = 0.169 \pm 0.0361$ (or $L_{900}/L_{1500}(\text{obs}) = 0.069 \pm 0.0137$, without the IGM correction) as an upper limit, given the aforementioned caveats. The labels, out and obs, adopt the convention in Steidel et al. (2018) and Pahl et al. (2021, 2023). The second L_{1500} estimate simply uses the weighted biweight luminosity density of the 113 wavelength bins between 1475 and 1525 \AA taken directly from the $2.6 < z < 3.5$ stack using the same method as L_{900} described earlier. This result differs by $\ll 1\%$, completely consistent with the first estimate. Repeating the same computation, but substituting the median and standard deviation for the weighted biweight location and biweight scale, yields an IGM transmission corrected $L_{900}/L_{1500}(\text{out}) = 0.159 \pm 0.0455$, or $L_{900}/L_{1500}(\text{obs}) = 0.066 \pm 0.0172$ when not correcting for the IGM.

To place this measurement in some context, we compare against the stack of the subset (26 out of 124 galaxies) of the LBG-selected, $z \sim 3$ galaxies in the Keck Lyman Continuum Spectroscopic Survey (KLCS; Steidel et al. 2018) that are also classical LAEs with ($W_{\lambda}(\text{Ly}\alpha) > 20 \text{ \AA}$) (Pahl et al. 2021). The overplotted stacks are presented in Figure 11. Both stacks are normalized to their own flux near 1500 \AA and interpolated onto the same wavelength grid and smoothed with a 1 pixel (0.44 \AA) Gaussian kernel (σ). The HETDEX (HPSC-1) stack has also been shifted to correct for its approximate 250 km s^{-1} $\text{Ly}\alpha$ velocity offset (Section 4.3). Though the individual spectra contributing to the KLCS stack are of higher S/N with longer exposures, they have similar resolving powers, with $R \sim 800$

for HETDEX and for KLCS at $\lambda < 5000 \text{ \AA}$ and $R \sim 1400$ for KLCS at $\lambda > 5000 \text{ \AA}$ (Steidel et al. 2018; Gebhardt et al. 2021). Our L_{900}/L_{1500} estimates are defined in a similar way as the $\langle f_{900}/f_{1500} \rangle_{\text{out}}$ measurements of Steidel et al. 2018; Pahl et al. 2021 and others.

As a brief aside, the $\text{Ly}\alpha$ troughs (Section 4.4) shown in the HPSC-1 stack are much deeper than in the KLCS stack. The KLCS LAE subsample is comprised of UV-bright, LBG-selected galaxies with weaker $\text{Ly}\alpha$, as compared to the majority of the 50,000 HPSC-1 LAEs. This difference in selection may probe galaxies with somewhat different halo and internal properties which could contribute to some differences in the troughs. However, as discussed in L. Weiss et al. (2023, in preparation) and briefly in Section 4.4, while the existence of the $\text{Ly}\alpha$ troughs is physically motivated, their manifestation within the HPSC-1 stack is substantially enhanced by the HETDEX data-reduction pipeline.

While our relative Lyman continuum values, $L_{900}/L_{1500}(\text{out})$, are $\sim 1.5\text{--}2.0 \times$ higher than what is found in Pahl et al. (2021) and Pahl et al. (2023) for the galaxies in their highest ($W_{\lambda}(\text{Ly}\alpha) > 20 \text{ \AA}$) equivalent width bin, based on a comparison to the properties of the HPSC-1 sample, we might expect a larger escape of Lyman continuum photons. Additionally, the $z \geq 3$ for $\sim 900 \text{ \AA}$ rest-frame IGM transmission in the model used in this work (Boquien et al. 2019) is about 10% higher than that in Steidel et al. (2018) and Pahl et al. (2021), making the IGM correction here slightly smaller. As can be seen in Figure 11, the equivalent width of the HPSC-1 $\text{Ly}\alpha$ line is roughly $3 \times$ larger than that of the KLCS LAE subsample, with HPSC-1 measuring 114 \AA (or 130 \AA for the $3.0 < z < 3.5$ subsample, see Table 1) and the KLCS LAE subsample measuring 36 \AA using the same MCMC fitting code used in Section 4.6. Measuring the UV continuum slope as in Section 4.7, we find the KLCS subsample stack with a shallower, but still very blue, $\beta = -1.88$ versus the -2.36 of the HPSC-1 stack. The FiCUS analyses for the KLCS subsample stack, with the same configurations as in Section 4.9, suggest a similarly young stellar population component with similar metallicity but a somewhat larger $E(B - V)$ as compared to the HPSC-1 sample. Using the SB99+SMC configuration, though all 4 runs show the same relative differences, we see the UV light-weighted average stellar age $= 9.36 \pm 1.39 \text{ Myr}$, $Z(Z_{\odot}) = 0.21 \pm 0.02$, and $E(B - V) = 0.052 \pm 0.001$.

Both the KLCS and the HPSC-1 LAEs show consistent ages for their recent star formation as well as comparable metallicities, suggesting similar ionizing photon production. However, the stronger Ly α emission, lower $E(B - V)$, and steeper UV β slope in the HPSC-1 sample promote the expectation of increased leakage of those photons from the HPSC-1 LAEs (Behrens et al. 2014; Verhamme et al. 2015; Smith et al. 2018; Calabro et al. 2021; Naidu et al. 2021; Chisholm et al. 2022; Maji et al. 2022; Saldana-Lopez et al. 2022).

We emphasize that, while this relative L_{900}/L_{1500} measurement can be used in context with other works, it is only a step in obtaining an estimate of the average, intrinsic escape fraction of ionizing photons from these galaxies. We also caution again (see Section 4.1) that the HPSC-1 sample is not as strictly controlled for contamination from on-sky neighbors as in Pahl et al. (2021) and that may influence the results. The subtraction of the average empty aperture (Section 3.2) helps compensate for contributions of light from faint interlopers, but there is no exclusion of LAEs with detected, sky-adjacent neighbors as in Davis et al. (2021) nor is there any deblending of light from such neighbors as is performed in D. Davis et al. (2023, in preparation). As such, this result is an upper limit. A more complete and extended study of the Lyman continuum escape from $z > 3$ LAEs will be presented in D. Davis et al. (2023, in preparation).

5. Summary

We have taken the 50,000 low spectral resolution ($R \sim 800$), generally low S/N LAE spectra (Ly α S/N ~ 6 , continuum S/N $\ll 1$) from the HETDEX Public Source Catalog 1 (Mentuch Cooper et al. 2023), applied a $\sim 1\%$ level correction for residual light, and stacked those spectra in the rest frame using the weighted biweight method. This procedure increased the spectral S/N by factors of several hundred and revealed a variety of otherwise noise-obscured features associated with LAEs. In stacking these large numbers of spectra, we marginalize over lines of sight, IGM transmission, galaxy orientation, and star formation stochasticity to yield a generally robust description of the average or typical member of the set, though at the loss of peculiar features of individual members. The Ly α luminosity (Section 4.5), equivalent width (Section 4.6), and g magnitude of the stack (and redshift-based substacks), are consistent with the corresponding median values of the LAE distribution, supporting the view of the stack as a valid average representation (Section 4.2).

The stack shows negative, asymmetric troughs (Section 4.4) to either side of the Ly α emission line. While real physics is behind the existence of the troughs, they are artificially enhanced by the HETDEX data-reduction pipeline and are excluded in the analyses of this work. L. Weiss et al. (2023, in preparation) will explore the physics of the troughs and the HETDEX pipeline updates that address them.

The HETDEX LAE stack is a bit bluer with stronger Ly α emission and less dust than the continuum-selected LAE stack from KLCS (Section 4.10 and Figure 11), but overall, is remarkably similar.

We find that the properties of stacked spectra show our average $z \sim 2.6$ LAE is very blue (UV $\beta \sim -2.4$) with a significant light contribution from a young, metal-poor stellar population (most of the UV light from stars with ages of 5–15 Myr, $Z \sim 0.2 Z_{\odot}$, with strong P Cygni profiles and weak metal absorption). The steep

UV β , low dust attenuation ($E(B - V) < 0.1$), strong Ly α emission ($\log L_{\text{Ly}\alpha} \sim 42.8$, $W_{\lambda}(\text{Ly}\alpha) \sim 114 \text{ \AA}$), and substantial $L_{900}/L_{1500}(\text{out})$ ($\lesssim 17\%$) all suggest a high intrinsic escape fraction of ionizing radiation. This supports the idea that the higher redshift analogs of the HETDEX LAEs could be major drivers of reionization.

Forthcoming research will expand and improve on these analyses with larger and more carefully curated LAE samples that will allow for finer binning and better exploration of the ensemble properties and their evolutions.

Acknowledgments

HETDEX is led by the University of Texas at Austin McDonald Observatory and Department of Astronomy with participation from the Ludwig-Maximilians-Universität München, Max-Planck-Institut für Extraterrestrische Physik (MPE), Leibniz-Institut für Astrophysik Potsdam (AIP), Texas A&M University, The Pennsylvania State University, Institut für Astrophysik Göttingen, The University of Oxford, Max-Planck-Institut für Astrophysik (MPA), The University of Tokyo, and Missouri University of Science and Technology. In addition to institutional support, HETDEX is funded by the National Science Foundation (grant AST-0926815), the State of Texas, the US Air Force (AFRL FA9451-04-2-0355), and generous support from private individuals and foundations.

Observations were obtained with the Hobby-Eberly Telescope (HET), which is a joint project of the University of Texas at Austin, the Pennsylvania State University, Ludwig-Maximilians-Universität München, and Georg-August-Universität Göttingen. The HET is named in honor of its principal benefactors, William P. Hobby and Robert E. Eberly.

VIRUS is a joint project of the University of Texas at Austin, Leibniz-Institut für Astrophysik Potsdam (AIP), Texas A&M University (TAMU), Max-Planck-Institut für Extraterrestrische Physik (MPE), Ludwig-Maximilians-Universität Muenchen, Pennsylvania State University, Institut für Astrophysik Göttingen, University of Oxford, and the Max-Planck-Institut für Astrophysik (MPA). In addition to institutional support, VIRUS was partially funded by the National Science Foundation, the State of Texas, and generous support from private individuals and foundations.

The authors acknowledge the Texas Advanced Computing Center (TACC) at The University of Texas at Austin for providing high-performance computing, visualization, and storage resources that have contributed to the research results reported within this paper. URL: <http://www.tacc.utexas.edu>

The Institute for Gravitation and the Cosmos is supported by the Eberly College of Science and the Office of the Senior Vice President for Research at the Pennsylvania State University.

K.G. acknowledges support from NSF-2008793. E.G. acknowledges support from NSF grant AST-2206222. A.S.L. acknowledges support from the Swiss National Science Foundation. S.S. acknowledges the support for this work from NSF-2219212. S.S. is supported in part by World Premier International Research Center Initiative (WPI Initiative), MEXT, Japan.

This research benefits from the open-source projects Python (Van Rossum & Drake 2009), astropy (Price-Whelan et al. 2018), NumPy (Harris et al. 2020), photutils (Bradley et al. 2020), and others in the open-source community.

ORCID iDs

Dustin Davis  <https://orcid.org/0000-0002-8925-9769>
 Karl Gebhardt  <https://orcid.org/0000-0002-8433-8185>
 Erin Mentuch Cooper  <https://orcid.org/0000-0002-2307-0146>
 William P. Bowman  <https://orcid.org/0000-0003-4381-5245>
 John Chisholm  <https://orcid.org/0000-0002-0302-2577>
 Robin Ciardullo  <https://orcid.org/0000-0002-1328-0211>
 Maximilian Fabricius  <https://orcid.org/0000-0002-7025-6058>
 Daniel J. Farrow  <https://orcid.org/0000-0003-2575-0652>
 Steven L. Finkelstein  <https://orcid.org/0000-0001-8519-1130>
 Caryl Gronwall  <https://orcid.org/0000-0001-6842-2371>
 Eric Gawiser  <https://orcid.org/0000-0003-1530-8713>
 Gary J. Hill  <https://orcid.org/0000-0001-6717-7685>
 Ulrich Hopp  <https://orcid.org/0000-0003-1008-225X>
 Lindsay R. House  <https://orcid.org/0000-0002-1496-6514>
 Donghui Jeong  <https://orcid.org/0000-0002-8434-979X>
 Wolfram Kollatschny  <https://orcid.org/0000-0002-0417-1494>
 Eiichiro Komatsu  <https://orcid.org/0000-0002-0136-2404>
 Chenxu Liu  <https://orcid.org/0000-0001-5561-2010>
 Maja Lujan Niemeyer  <https://orcid.org/0000-0002-6907-8370>
 Alberto Saldana-Lopez  <https://orcid.org/0000-0001-8419-3062>
 Shun Saito  <https://orcid.org/0000-0002-6186-5476>
 Donald P. Schneider  <https://orcid.org/0000-0001-7240-7449>
 Jan Snigula  <https://orcid.org/0000-0003-4044-5357>
 Sarah Tuttle  <https://orcid.org/0000-0002-7327-565X>
 Laurel H. Weiss  <https://orcid.org/0000-0002-4974-1243>
 Gregory Zeimann  <https://orcid.org/0000-0003-2307-0629>

References

Adams, J. J., Blanc, G. A., Hill, G. J., et al. 2011, *ApJS*, 192, 5
 Aghanim, N., Akrami, Y., & (Planck Collaboration) 2020, *A&A*, 641, A1
 Balestra, I., Mainieri, V., Popesso, P., et al. 2010, *A&A*, 512, A12
 Bassett, R., Ryan-Weber, E. V., Cooke, J., et al. 2022, *MNRAS*, 511, 5730
 Beals, C. S. 1934, *Obs*, 57, 319
 Beers, T. C., Flynn, K., & Gebhardt, K. 1990, *AJ*, 100, 32
 Behrens, C., Byrohl, C., Saito, S., & Niemeyer, J. C. 2018, *A&A*, 614, A31
 Behrens, C., Dijkstra, M., & Niemeyer, J. C. 2014, *A&A*, 563, A77
 Berry, M., Gawiser, E., Guaita, L., et al. 2012, *ApJ*, 749, 4
 Boquien, M., Burgarella, D., Roehlly, Y., et al. 2019, *A&A*, 622, A103
 Bouwens, R. J., Illingworth, G. D., Oesch, P. A., et al. 2010b, *ApJL*, 708, L69
 Bradley, L., Sipőcz, B., Robitaille, T., et al. 2020, astropy/photutils: v1.0.0, Zenodo, doi:10.5281/zenodo.4044744
 Byrohl, C., & Gronke, M. 2020, *A&A*, 642, L16
 Byrohl, C., Saito, S., & Behrens, C. 2019, *MNRAS*, 489, 3472
 Calabro, A., Castellano, M., Pentericci, L., et al. 2021, *A&A*, 646, A39
 Calzetti, D. 2001, *PASP*, 113, 1449
 Chisholm, J., Rigby, J. R., Bayliss, M., et al. 2019, *ApJ*, 882, 182
 Chisholm, J., Saldana-Lopez, A., Flury, S., et al. 2022, *MNRAS*, 517, 5104
 Ciardullo, R., Gronwall, C., Wolf, C., et al. 2011, *ApJ*, 744, 110
 Davis, D., Gebhardt, K., Mentuch Cooper, E., et al. 2021, *ApJ*, 920, 122
 Davis, D., Gebhardt, K., Mentuch Cooper, E., et al. 2023, *ApJ*, 946, 86
 Dijkstra, M., Lidz, A., & Wyithe, J. S. B. 2007, *MNRAS*, 377, 1175
 Eldridge, J. J., Stanway, E. R., Xiao, L., et al. 2017, *PASA*, 34, e058
 Erb, D. K., Steidel, C. C., Trainor, R. F., et al. 2014, *ApJ*, 795, 33
 Feltre, Anna, Maseda, Michael, V., Bacon, Roland, et al. 2020, *A&A*, 641, A118
 Finkelstein, S. L. 2010, in ASP Conf. Ser. 432, New Horizons in Astronomy: Frank N. Bash Symp. 2009, ed. L. M. Stanford et al. (San Francisco, CA: ASP), 33
 Gawiser, E., Francke, H., Lai, K., et al. 2007, *ApJ*, 671, 278
 Gebhardt, K., Mentuch Cooper, E., Ciardullo, R., et al. 2021, *ApJ*, 923, 217
 Grazian, A., Giallongo, E., Gerbasi, R., et al. 2016, *A&A*, 585, A48
 Green, P. J., Schartel, N., Anderson, S. F., et al. 1996, *MNRAS*, 283, 1015
 Greisen, E. W., Calabretta, M. R., Valdes, F. G., & Allen, S. L. 2006, *A&A*, 446, 747
 Gronwall, C., Ciardullo, R., Hickey, T., et al. 2007, *ApJ*, 667, 79
 Guhathakurta, P., Tyson, J. A., & Majewski, S. R. 1990, *ApJL*, 357, L9
 Gurung-López, S., Orsi, A. A., Bonoli, S., et al. 2019, *MNRAS*, 491, 3266
 Gurung-López, S., Saito, S., Baugh, C. M., et al. 2020, *MNRAS*, 500, 603
 Harris, C. R., Millman, K. J., van der Walt, S. J., et al. 2020, *Natur*, 585, 357
 Heckman, T. M., Borthakur, S., Overzier, R., et al. 2011, *ApJ*, 730, 5
 Hill, G. J., Lee, H., MacQueen, P. J., et al. 2021, *ApJ*, 162, 298
 Hu, E. M., Cowie, L. L., Capak, P., & Kakazu, Y. 2005, in IAU Symp. 199, Probing Galaxies through Quasar Absorption Lines, ed. P. R. Williams, C.-G. Shu, & B. Menard (Cambridge: Cambridge Univ. Press), 363
 Inoue, A. K., Shimizu, I., Iwata, I., & Tanaka, M. 2014, *MNRAS*, 442, 1805
 Izotov, Y. I., Schaerer, D., Thuan, T. X., et al. 2016, *MNRAS*, 461, 3683
 Izotov, Y. I., Worseck, G., Schaerer, D., et al. 2018, *MNRAS*, 478, 4851
 Jaskot, A. E., & Oey, M. S. 2014, *ApJL*, 791, L19
 Kerutt, J., Wisotzki, L., Verhamme, A., et al. 2022, *A&A*, 659, A183
 Kirkby, D., Park, A., Moustakas, J., et al. 2023, desihub/speclite, v0.16, Zenodo, doi:10.5281/zenodo.7734526
 Kroupa, P. 2001, *MNRAS*, 322, 231
 Laursen, P., Sommer-Larsen, J., & Razoumov, A. O. 2011, *ApJ*, 728, 52
 Leitet, E., Bergvall, N., Hayes, M., Linné, S., & Zackrisson, E. 2013, *A&A*, 553, A106
 Leitherer, C., Leão, J. R. S., Heckman, T. M., et al. 2001, *ApJ*, 550, 724
 Leitherer, C., Ortiz Otálvaro, P. A., Bresolin, F., et al. 2010, *ApJS*, 189, 309
 Liu, C., Gebhardt, K., Mentuch Cooper, E., et al. 2022, *ApJS*, 261, 24
 Lujan Niemeyer, M., Komatsu, E., Byrohl, C., et al. 2022, *ApJ*, 929, 90
 Madau, P., Ferguson, H. C., Dickinson, M. E., et al. 1996, *MNRAS*, 283, 1388
 Maji, M., Verhamme, Anne, Rosdahl, Joakim, et al. 2022, *A&A*, 663, A66
 Marchi, F., Pentericci, L., Guaita, L., et al. 2017, *A&A*, 601, A73
 Meiksin, A. 2006, *MNRAS*, 365, 807
 Mentuch Cooper, E., Gebhardt, K., Davis, D., et al. 2023, *ApJ*, 943, 177
 Muzahid, S., Schaye, J., Marino, R. A., et al. 2020, *MNRAS*, 496, 1013
 Naidu, R. P., Matthee, J., Oesch, P. A., et al. 2021, *MNRAS*, 510, 4582
 Nilsson, K. K., & Meisenheimer, K. 2009, *NewAR*, 53, 37
 Pahl, A. J., Shapley, A., Steidel, C. C., et al. 2023, *MNRAS*, 521, 3247
 Pahl, A. J., Shapley, A., Steidel, C. C., Chen, Y., & Reddy, N. A. 2021, *MNRAS*, 505, 2447
 Prevot, M. L., Lequeux, J., Maurice, E., Prevot, L., & Rocca-Volmerange, B. 1984, *A&A*, 132, 389
 Price-Whelan, A. M., Sipőcz, B. M., (Astropy Collaboration), et al. 2018, *AJ*, 156, 123
 Ramsey, L. W., Adams, M. T., Barnes, T. G., et al. 1998, *Proc. SPIE*, 352, 34
 Reddy, N. A., Steidel, C. C., Pettini, M., Bogosavljević, M., & Shapley, A. E. 2016, *ApJ*, 828, 108
 Saldana-Lopez, A., Schaerer, D., Chisholm, J., et al. 2023, *MNRAS*, 529, 6295
 Salim, S., Boquien, M., & Lee, J. C. 2018, *ApJ*, 859, 11
 Shapley, A. E., Steidel, C. C., Pettini, M., & Adelberger, K. L. 2003, *ApJ*, 588, 65
 Shapley, A. E., Steidel, C. C., Pettini, M., Adelberger, K. L., & Erb, D. K. 2006, *ApJ*, 651, 688
 Shibuya, T., Ouchi, M., Nakajima, K., et al. 2014, *ApJ*, 788, 74
 Shvaić, I., Reddy, N., Rieke, G., et al. 2020, *ApJ*, 899, 117
 Smith, A., Kannan, R., Tacchella, S., et al. 2022, *MNRAS*, 517, 1
 Smith, A., Ma, X., Bromm, V., et al. 2018, *MNRAS*, 484, 39
 Steidel, C. C., Bogosavljević, M., Shapley, A. E., et al. 2018, *ApJ*, 869, 123
 Steidel, C. C., Giavalisco, M., Pettini, M., Dickinson, M., & Adelberger, K. L. 1996, *ApJ*, 462, L17
 Van Rossum, G., & Drake, F. L. 2009, Python 3 Reference Manual (Scotts Valley, CA: CreateSpace)
 Vargas, C. J., Bish, H., Acquaviva, V., et al. 2014, *ApJ*, 783, 26
 Verhamme, A., Garel, T., Ventou, E., et al. 2018, *MNRAS*, 478, L60
 Verhamme, A., Orlitová, I., Schaerer, D., & Hayes, M. 2015, *A&A*, 578, A7
 Verhamme, A., Schaerer, D., & Maselli, A. 2006, *A&A*, 460, 397
 Zheng, Z., Cen, R., Trac, H., & Miralda-Escudé, J. 2010, *ApJ*, 726, 38